Space Sci Rev (2007) 132: 291–306
DOI 10.1007/s11214-007-9231-1

The Surface of Mercury as Seen by Mariner 10

G. Cremonese · A. Sprague · J. Warell · N. Thomas · L. Ksamfomality

Received: 22 December 2006 / Accepted: 4 June 2007 / Published online: 4 October 2007

Abstract The Mariner 10 spacecraft made three flyby passes of Mercury in 1974 and 1975. It imaged a little less than half of the surface and discovered Mercury had an intrinsic magnetic field. This paper briefly describes the surface of Mercury as seen by Mariner 10 as a backdrop to the discoveries made since then by ground-based observations and the optimistic anticipation of new discoveries by MESSENGER and BepiColombo spacecraft that are scheduled for encounter in the next decade.

Keywords Planets: Mercury · Space vehicule · Instrumentation: imager · Mercury surface · Mariner 10

1 Introduction

This paper is devoted to the description of Mercury's surface as seen by Mariner 10. Mariner 10 imaged just less than half of the surface. From those images we learned that Mercury is a heavily cratered planet with an ancient surface that dates back to a period before accretionary heat was fully dissipated as evidenced by a scarp system that indicates global contraction.

G. Cremonese (✉)
INAF-Osservatorio Astronomico, vic. Osservatorio 5, 35122 Padova, Italy
e-mail: gabriele.cremonese@oapd.inaf.it

A. Sprague
Lunar and Planetary Laboratory, University of Arizona, Tucson, AZ 85721, USA

J. Warell
Dept. Astronomy & Space Phys., Uppsala University, Uppsala, Sweden

N. Thomas
Physikalisches Institut, University of Bern, Bern, Switzerland

L. Ksamfomality
IKI, Moscow, Russia

Mercury poses severe thermal and dynamical challenges to observation by spacecraft, and to date the planet has been visited by only one spacecraft, Mariner 10. The Mariner 10 mission was not intended to orbit Mercury because it would be travelling so fast past the planet (50 km/s) that it would require a huge amount of fuel to slow down the spacecraft enough to put into orbit. The size of the retrorocket would have to be equivalent to a medium-sized launch vehicle of that era. For almost 30 years we have waited for new technology to overcome the obstacles of cruise and orbital insertion to Mercury.

At last, two more missions are scheduled to encounter and orbit the planet in the next decade. MESSENGER, a NASA mission, launched on August 2004, will undergo orbital insertion in March 2011. The European Space Agency (ESA) approved the new mission, Bepi-Colombo, to Mercury pointing to a cornerstone, the n.5. in the year 2000. BepiColombo, scheduled for launch in August 2013, will orbit the planet beginning in September 2019. In the meantime, ground-based observations of Mercury are systematically increasing our knowledge of this enigmatic planet. In order to better appreciate the new ground-based discoveries and the challenges and scientific goals of the MESSENGER and BepiColombo missions, we benefit from becoming familiar with the Mercury seen by Mariner 10.

2 The Mariner 10 Mission

The mission plan for Mariner 10 was the most complex for any planetary mission up to that time. A gravity-assist trajectory technique was needed to obtain an economically acceptable mission. This technique allows a spacecraft to change both its direction and speed without using a valuable fuel, thereby saving time and leaving more weight for the scientific payload. A single gravity-assist can provide more delta V than a full rocket stage.

In February 1970 the mechanical engineer Giuseppe Colombo, of the University of Padova, Italy, noted that after Mariner 10 flew by Mercury, its orbital period around the Sun would be quite close to twice Mercury's orbital period. Therefore, he suggested that a second planet encounter could therefore be accomplished. After having confirmed this suggestion, the JPL carefully selected the Mercury flyby points in order to get a gravity correction able to return to Mercury six months later. The number of flybys depended upon the fuel available for midcourse corrections and attitude control. Mariner 10 achieved three encounters with Mercury before running out of fuel. This strategy limited the view of Mercury's surface to the same half of the planet (longitudes 10–190°).

In the very narrow launch window, NASA chose November 3, 1973, so that the spacecraft encountered Mercury at a time when it could view the planet about half lit (quadrature). Viewing Mercury at this phase made it easier to distinguish surface features by their shadows. The trajectory relied on Venus's gravitational field to alter the spacecraft's flight path and causing it to fall closer to the Sun and cross Mercury's orbit at the precise time needed to encounter the planet.

The flight plan called for the upper-stage Centaur rocket to be turned off for 25 minutes shortly after launch from Kennedy Space Center. Then a second ignition thrust the Mariner spacecraft in a direction opposite to the Earth's orbital motion, providing the spacecraft with a lower velocity relative to the Sun than the Earth's orbital velocity. This allowed it to be drawn inward by the Sun's gravitational field and achieve an encounter with Venus. After a few months, Mariner 10 approached Venus from its night side, passing over the sunlit side and, slowed by Venus's gravitational field, falling inward toward the Sun to rendezvous with Mercury.

The Mariner 10 spacecraft evolved from more than a decade of Mariner technology, beginning with the Venus mission in 1962 and culminating with the Mars orbiter in 1971.

Mariner 10 would be the last of the Mariner spacecraft to fly. Like the other Mariners, it consisted of an octagonal main structure, solar cell panels, a battery for electrical power, nitrogen gas jets for three-axis attitude stabilization and control, star and Sun sensors for celestial reference, S-band radio (12.6 cm wavelength) for command and telemetry, a high- and low-gain antenna, and a hydrazine rocket propulsion system for trajectory corrections.

The weight of the spacecraft was 534 kg, including 29 kg of hydrazine and 30 kg for the adapter to the launch vehicle. The scientific payload had a mass of 78 kg. The Mariner project modified the spacecraft for a specific mission toward Mercury because it had to approach the Sun at the closest distance ever achieved by a spacecraft. It was subjected to insolation up to 4.5 times greater than at Earth, requiring thermal control to maintain temperatures at a level that would not damage the spacecraft systems. As the spacecraft approached the Sun, the panels were rotated to change the angle at which light fell on them to maintain a suitable temperature of about 115°C.

Mariner 10 was able to handle up to 118 kb/s of imaging data and 2,450 bit/s for any other data, using a X-band antenna and the capability of transmitting telemetry on both X and S bands.

2.1 The Imaging System

The Mariner 10 imaging system consisted of two vidicon cameras, each with an eight-position filter wheel. The vidicons were attached to long focal length Cassegrain telescopes, which were mounted on a scan platform for accurate pointing. These telescopes provided narrow-angle and high resolution images.

The design team came up with an attractive, but risky, solution: treble the focal length of the Mariner 6/7 design and use twin camera systems on alternate 42-second readout cycles. This way, many high-resolution images under good low lighting could be captured well before and well after passing the darkened surface at closest approach. In addition, the TV team was able to persuade the telemetry engineers at JPL that television images can be quite interpretable even with considerable “salt-and-pepper” telemetry noise. Hence, the communication bandwidth for Mariner 10 could be increased greatly within existing power and antenna capabilities by accepting a much higher noise level. This meant that in addition to acquiring a full tape recorder, as had the earlier Mars Mariners, Mariner 10 could also transmit the 115,000-bps output video signal directly to Earth during many intervals. As a consequence, Mariner 10 would return many thousands of extraordinarily sharp images of Mercury, rather than the few hundred lower-resolution frames that otherwise would have been the case. Trebling the focal length of an existing optical design is never easy, but in this case the team was constrained as well for volume and configuration reasons to keep the rather short overall length (550 mm) of the Mariner 6/7 telescope nearly the same for Mariner 10. Thus, the increase in focal length from 500 to 1500 mm had to be accomplished entirely by secondary mirror magnification at the front of the telescope, where there would maximum vulnerability to thermal gradients.

The primary objective of the imaging experiment was to study the physiography and geology of Mercury’s surface; determine accurately its size, shape, and rotation period; evaluate its photometric properties; and search for possible satellites and color differences on its surface.

The vidicon imaging system was spatially nonuniform in bias and dark current, as well as being nonlinear at the extremes of the light transfer curve. Prelaunch flat-field images acquired at varying exposure times allowed for the derivation of a nonlinearity and sensitivity nonuniformity correction, while an average of inflight images of deep space corrected for system offset.

Table 1 Main characteristics of the vidicon cameras

Focal length	1500 mm (62 mm)[a]
F ratio	f/8.4
Shutter velocity range	33.3 ms to 11.7 s
Field of view	0.38° × 0.47° (9° × 11°)[a]
Vidicon target area	9.6 × 12.35 mm
Line scans per picture	700
Number of pixel per line	832
Number of bits per pixel	8
Filters and central wavelength	Clear (487 nm), UV (355 nm), blue (475 nm), minus UV (511 nm), orange (575 nm)

[a]Wide angle imaging

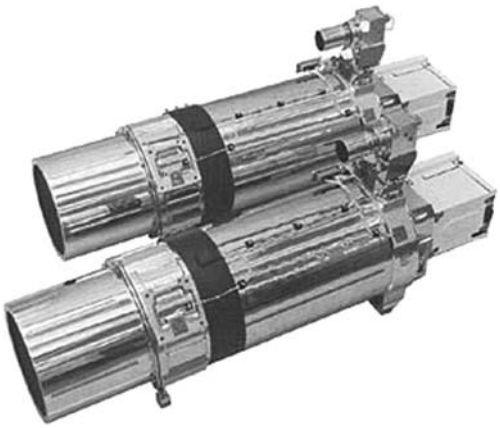

Fig. 1 Sketch of the vidicon cameras onboard Mariner 10

Table 1 shows the main characteristics of the imaging system, and Fig. 1 presents a sketch of the cameras.

During the three close encounters with Mercury in 1974–1975, the imaging system has acquired images of 40–45% of the total surface at spatial resolutions between 1 and 4 km/px, with highest resolutions obtained in selected areas down to about 100 m/px and due to the resonances of orbital encounter geometry the viewed longitude range was 10–190°.

3 Cratering

The global view of Mercury's surface, as revealed by the Mariner 10 camera during its first encounter (Mercury I) with the planet, at first glimpse appears lunar-like, covered with impact craters (Murray et al. 1974). Like the Moon, Mercury shows several large multi-ring structures, such as the Caloris basin whose eastern half was captured by Mariner 10 cameras. In both ways comparable to, but also different from the lunar surface, Mercury features vast smooth plains, in many places with a lower density of impact craters. Crater forms on Mercury are similar to their lunar counterparts (Spudis and Guest 1988).

On planetary surfaces we can see simple craters that are the smallest hypervelocity impact structures, they are bowl-shaped in form and have sharp rims and over-turned stratig-

raphy in the ejecta blanket. The morphology of these structures is controlled mainly by the strength of the substrate.

As impact energy increases, the target loses strength and there is a collapse of the walls and an uplift of the crater interior creating the complex craters. These are consequently formed in a regime where gravity is the dominant factor. Complex craters are characterized by terraced walls that are the surficial manifestation of subsurface faults, and they also show central peaks that contain material brought up from deep beneath the crater. They have smaller depth-to-diameter ratios because the increased importance of gravity collapse results in more uplift of floor. In these craters the average depth is about one-tenth of the diameter.

The next morphological step up in the energy scale corresponds to basins, which transition from structures that have a central peak and rings, peak-ring basins, to no central peak and multiple rings, multi-ring basins. In the transition to a peak ring basin, the central peak collapses to form a small ring that increases with increasing impact kinetic energy. In a multi-ring basin the number of rings scales with the impact energy and the mechanical properties of the near-surface layer into which the impact occurred. Basins have even smaller depth-to-diameter ratios than complex craters due to more central uplift.

As for simple-complex craters, the diameter of the complex crater-to-basin transition also depends on gravity, but the morphology of large multi-ring basins cannot be attributed to gravity alone.

The transition diameter from simple to complex crater forms on Mercury is 10.3 km (Pike 1988). In contrast to lunar craters, however, continuous ejecta and secondary crater fields are rarely found on Mercury, due to the higher surface gravity (Gault et al. 1975).

However, impact debris re-impacts the surface with higher velocities and hence has a stronger effect on eroding pre-existing landforms (Gault et al. 1975; Spudis and Guest 1988).

In detail, Mercury's craters have morphological differences from those on the Moon and Mars, partly due to differences in gravity and impactor environment (e.g., higher velocity impacts on Mercury), but most of the differences are probably due to the different geological processes that erode and degrade craters after they have formed on the various planets.

Potential sources for the impactors that formed Mercury's craters are numerous. In principle, the size distributions and the impact rates could have varied with time and in ways not necessarily correlated with the cratering histories of other bodies. Sources include: the Near-Earth asteroids and their cousins (of which only three have yet been found), which orbit entirely interior to Earth's orbit (termed Apoheles); short- and long-period comets, including sun-grazers; vulcanoids, an as-yet-undiscovered hypothetical population of remnant planetesimals from accretionary epochs, orbiting mainly inside Mercury's orbit; and secondary cratering by ejecta from basins and large primary craters. Endogenic crater-forming processes (e.g., volcanism) are also possible.

Interesting crater studies of Mercury can be based on topographic information derived from the shadows of craters in the Mariner 10 images in order to get the depth-to-diameter ratio. This ratio can be used for investigating if terrain types may be related to different values.

Figure 2 shows two examples of measurements of depth and diameter of craters according to Pike (1988), who collected morphologic characteristics of 316 impact craters, and Andre' and Watters (2006) who analyzed 173 craters.

Craters can be used as relative age markers by counting their numbers and size distributions on a planetary surface. To use craters in the dating of surfaces one must consider the rate of crater production and obliteration. To assess the crater population, the principal piece of information is the measured number of craters as a function of diameter over planetary surfaces over all ages. The principal piece of information in crater counting is the number of craters per unit area as a function of diameter.

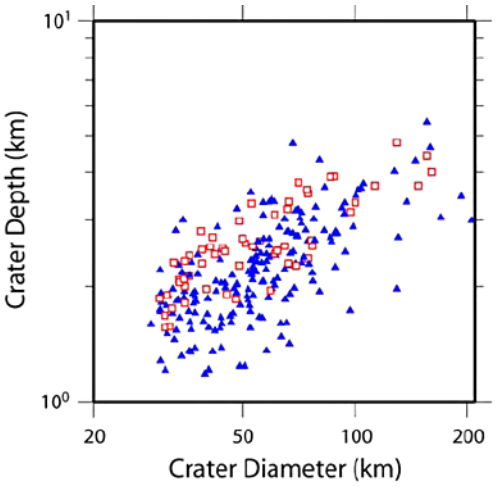

Fig. 2 Log–log plot of the depths and diameters of mature complex hermean craters. *Blue triangles* represent data from Andre' and Watters (2006) and *red squares* represent data from Pike (1988)

Neukum (1983) and Neukum and Ivanov (1994) proposed an analytical function to describe the cumulative number of craters with diameters larger than a given diameter D per unit area. This function was constructed from pieces of impact crater-size-frequency distribution (SFD) data measured in different areas of various ages on the Moon. Hence, the Neukum production function (NPF) implicitly assumes a constant shape of the production SFD during all lunar history (Neukum et al. 2001).

The well-investigated size-frequency distributions for lunar craters may be used to estimate the SFD for projectiles which formed craters on terrestrial planets and on asteroids (Neukum et al. 2001). The result shows the relative stability of these distributions during the past 4 Gyr. The derived projectile size-frequency distribution is found to be very close to the size-frequency distribution of Main-Belt asteroids as compared with the recent Spacewatch asteroid data and astronomical observations as well as data from close-up imagery by space missions (Ström et al. 2005). It means that asteroids (or, more generally, collisionally evolved bodies) are the main component of the impactor family. A cratering chronology model is established that can be used as a safe basis for modelling the impact chronology of other terrestrial planets, especially Mercury (Ivanov 2001; Hartmann and Neukum 2001).

The general conclusion from some models is that the impact cratering rate on Mercury does not seem to differ more than $\pm 50\%$ from the lunar cratering rate in the same diameter bins. However, the shift of crater diameters and diameters of strength/gravity and simple/complex crater transition change the shape of the Mercurian production function in comparison with the lunar PF (Strom et al. 1975).

Figure 3 reports an example of few impact cratering chronology models, as discussed by Neukum et al. (2001).

Wagner et al. (2001) carried out new crater size–frequency measurements on the Mariner 10 images for various geologic units, using a recently updated crater production function polynomial and impact cratering chronology model derived for Mercury (e.g. Ivanov et al. 2001), in order to reassess the time-stratigraphic system established (McCauley et al. 1981; Spudis and Guest 1988).

The geologic units identified are: the densely cratered terrain (highlands), craters and basins, as the Caloris that is the youngest and largest one (about 1300 km in diameter) known so far. The results are reported in Table 2.

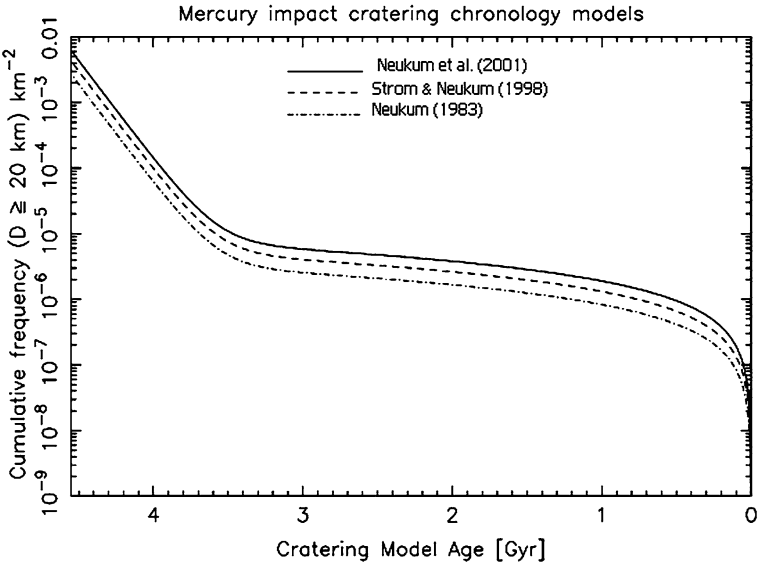

Fig. 3 Mercury impact cratering chronology model discussed by Neukum et al. (2001), compared to models published earlier (Neukum 1983; Ström and Neukum 1988). Cumulative frequency for $D \geq 20$ km plotted versus cratering model age in Giga-years (Gyr)

Table 2 Cumulative frequencies (for $D > 10$ km) and associated cratering model ages for major geologic units, craters and basins. Older values from (Ström and Neukum 1988) compared to updated values (Wagner et al. 2001). Uncertainties for cumulative frequencies (Ström and Neukum 1988; Wagner et al. 2001) are on the order of 20–30%, translating into model age uncertainties of 0.03–0.06 Gyr (Ström and Neukum 1988; Wagner et al. 2001)

Geologic unit	Cum. frequency ($D > 10$ km)		Crat. model age (Gyr)	
	Ström and Neukum (1988)	Wagner et al. (2001)	Ström and Neukum (1988)	Wagner et al. (2001)
Kuiper	–	(4.04e-6)	–	(1.0)
Mansur	–	(2.31e-5)	–	(3.5)
Caloris	6.85e-5	7.51e-5	3.85	3.77 ± 0.06
Beethoven	1.53e-4	1.22e-4	3.98	3.86 ± 0.05
Tolstoj	2.65e-4	2.51e-4	4.06	3.97 ± 0.05
Pushkin	3.45e-4	2.72e-4	4.10	3.98 ± 0.06
Haydn	3.65e-4	2.76e-4	4.11	3.99 ± 0.06
Dostojewskij	5.49e-4	2.75e-4	4.17	3.99 ± 0.06
Chekhov	4.04e-4	4.15e-4	4.12	4.05 ± 0.08
Highlands	5.99e-4	4.81e-4	4.18	4.07 ± 0.03

4 Global Contraction and Tectonics

One of the most important results of Mariner 10's imaging was the discovery that Mercury exhibits tectonic features. These features indicate Mercury's global contraction and provide enough geologic evidence to place the event at the end of the late heavy bombardment of

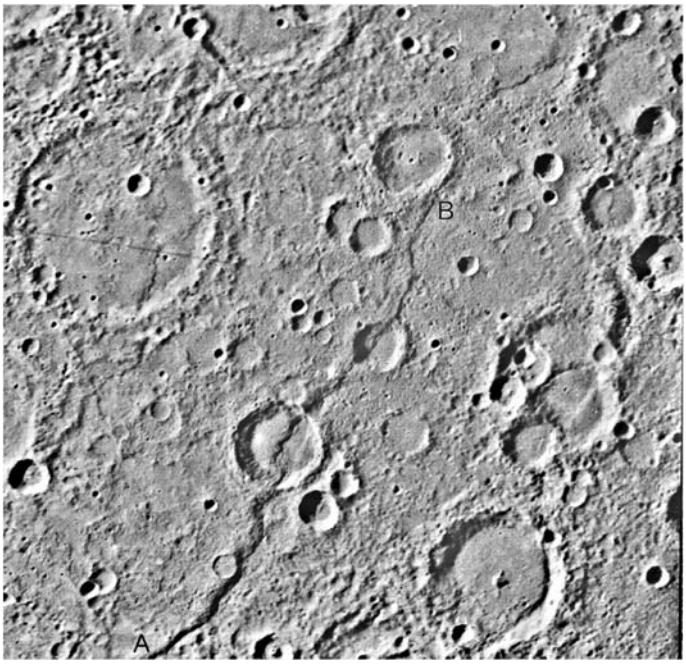

Fig. 4 Discovery fault discovered in Mariner 10 images during the third encounter in 1975. It traverses Mercury's surface for about 400 kilometers (measured from A to B) and has scarp faces of up to 1.5 km high. Figure from Strom and Sprague (2003)

the inner solar system and continuing until after the smooth intercrater plains formed (about 3.8 billion years ago) (Strom et al. 1975). The most obvious evidence discovered in Mariner 10 imagery was a long, sinuous scarp system extending for more than hundreds of km over Mercury's surface. Cliffs along the scarp appear to be 1.5 to 3 km high at some locations. The scarps cut crater rims (Fig. 4) and other landforms in such a way that permits us to be certain that they are a result of thrust faulting on a huge scale. The cliffs are rounded and in some cases have deformed the land forms they transect. Almost every region imaged by Mariner 10 shows examples of lobate scarps that were emplaced after the heavy bombardment and formation of the intercrater plains. The extensive system of thrust faults indicates that Mercury underwent a period of contraction that resulted in a decrease in surface area estimated to be about 31,000 to 63,000 km^2 following a shrinking diameter of 1–2 km (Strom et al. 1975).

Scarps younger than the emplacement of the intercrater plains have been identified, in particular, in pre-Tolstojan intercrater plains and Tolstojan and Calorian smooth plains units (Watters et al. 2004). This indicates that contraction associated with core formation and cooling continued throughout this period.

Another important tectonic discovery resulting from study of Mariner 10 images was evidence of a change in the shape of Mercury's lithosphere as a result of tidal despinning (cf. Melosh and McKinnon 1988). The evidence is a grid of lineaments (valleys, ridges, scarps, linear portions of central peaks, etc.) that roughly trends from the Caloris Basin antipode around to the Caloris Basin (Thomas et al. 1988). The formation of the grid is proposed to follow in two steps. First, the change in the surface area during global contraction caused a system of thrust faults while tidal despinning of the planet created various lineament struc-

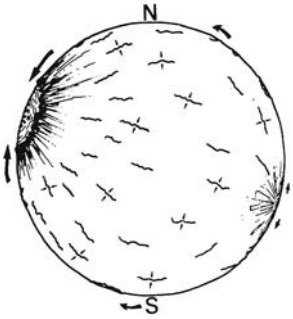

Fig. 5 Lateral flow of Mercury's lithosphere radially toward the center of Caloris Basin as basin melt cooled and subsided may have imprinted the lineament trend seen at Mercury. Figure adapted from Thomas et al. (1988)

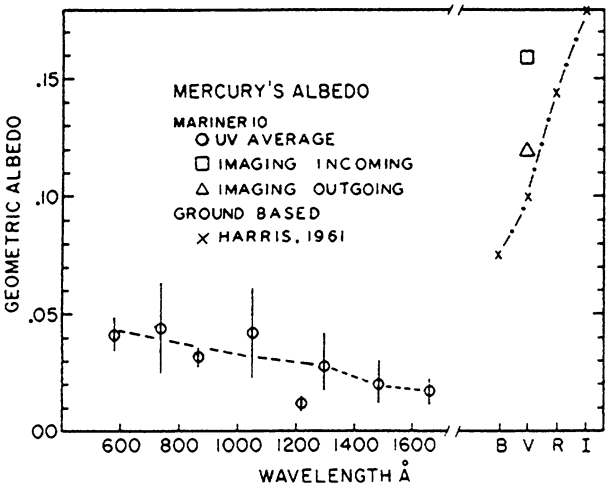

Fig. 6 The EUV albedo (*circles with error bars*) of Mercury measured in eight bands by the UV instrument on Mariner 10. The BVRI measurements at right are from Harris (1961) with boxes from incoming and outgoing Mariner 10 images

tures because of changes in shape of the lithosphere (Melosh and McKinnon 1988). Then, as illustrated by Fig. 5, the stretching of the lithosphere toward the center of the Caloris Basin following its formation, imprinted the grid trend (Thomas et al. 1988).

The part of the global system of thrust faults seen by Mariner 10 and the high relief ridges associated with them have been analyzed with respect to azimuthal and spatial distribution to constrain thermal models and to determine the origin of tectonic stresses (Melosh and McKinnon 1988). Some trends in the faults, lineaments and other features do not seem to be associated with despinning but rather with long-lived tectonic uplift bulge resulting in horst and graben extentional features in the Tolstoj-Zeami region (Thomas 1997). The implication of these features is that they are associated with a deep and long-lived, large-scale internal activity (Thomas 1997).

Other tectonic structures are also present. Following the excavation of Caloris Basin (and the lithospheric flow radially toward the basin center), basin concentric and basin radial ridges formed in response to basin interior lavas undergoing subsidence and compression (Watters et al. 2004). Wrinkle ridges formed as surface area decreased. Transecting the wrinkle ridges is a network of polygonal troughs exhibiting characteristics of graben formed from extensional stresses introduced by basin floor uplift (cf. Melosh and McKinnon 1988).

Recent modeling indicates that during the time of floor uplift, Mercury's crustal thickness must have already been thick enough to prevent the graben network destruction (Watters et al. 2004).

Regional thrust faults have been used to estimate the elastic lithospheric thickness given model assumptions regarding compositional and thermal physical parameters. Remarkably, models indicate the elastic lithosphere to be roughly 40 to 125 km (cf. Nimmo and Watters 2004 and references therein). Mercury's crust is estimated to be from 125 to 140 km thick, a range corresponding to a greater fraction of the total mantle volume than the Moon, Mars or Venus (Nimmo and Watters 2004).

The hilly and hummocky terrain antipodal to Caloris Basin is another region of tectonic, geologic, and physical interest. Because it exists antipodal to the Caloris Basin and shows no preferential directional trends in the lineations transecting the region, it does not appear to be a region of either regional compression or extension. Rather, a plausible formation scenario is that the random blockiness is a result of the convergence of seismic waves following the impact forming Caloris Basin (Shultz and Gault 1974).

It is thought that Mercury is no longer tectonically active. The geologic evidence from Mariner 10 indicates that the planet ceased tectonism sometime after core formation and the emplacement of the intercrater plains, probably between 3.8 and 3.2 by ago.

5 Surface Scattering Properties

The surface scattering and material properties of Mercury were studied from ultraviolet-optical images and thermal infrared radiance data obtained with the Television Photography (Murray et al. 1974; Soha et al. 1975) and the Two-Channel Infrared Radiometer experiments (Chase et al. 1976).

In addition to a primary objective of morphologic mapping and geologic studies of the Mercurian surface, the television camera also provided flux calibrated image data from which scattering and compositional parameters were inferred. For these studies, the ultraviolet (355 nm) and orange (575 nm) filters, as well as a UV polarizing filter, were primarily employed.

5.1 Light-Scattering Properties

From the orange image data, Hapke et al. (1975) determined the average normal albedo of Mercury's surface to be 0.14 at 554 nm. Pointing angle constraints for Mariner 10 restricted the phase angle coverage to between 80 and 110 degrees, and photometric results were thus derived from disk images of the planet rather than phase curve data or a combination of both. Brightness scans across the luminance equator extracted from first encounter images of the incoming hemisphere, which was found to be primarily covered by intercrater plains, were very similar to brightness profiles of lunar highlands at corresponding phase angles which had previously been obtained with the same camera. Images of the outgoing hemisphere, covered with smooth plains at the terminator and intercrater plains near the limb, indicated that the photometric properties of smooth plains more closely resemble the lunar maria than heavily cratered highland units.

Normal albedos at 5 degree phase angle and 554 nm wavelength were calculated by Hapke et al. (1975) assuming that the lunar photometric function of Hapke (1966) was valid for all types of geologic units. The intercrater plains were found to have albedos of 0.14 which was similar to lunar highlands, while the somewhat darker smooth plains were

brighter than most lunar maria. Two types of smooth plains were found—bright plains with albedos of about 0.20, and dark plains in and around the Caloris basin with albedos of around 0.13. Immature ray craters were found to have albedos systematically higher than lunar examples, with values of 0.35 not uncommon, and with the floor of Kuiper being the brightest with a normal albedo of 0.45. These values are slightly higher, particularly for bright ray craters, than the normal albedos previously cited in the preliminary report by Murray et al. (1974).

A search for regions of anomalous relative linear polarization signal was performed by comparing the UV imaging and the UV polarizing filter images, having the polarization direction oriented in the principal scattering plane. Hapke et al. (1975) reported that no strongly polarizing regions could be found to a size limit of 20 km. Polarization differences across the surface were determined to be generally less than 15%, with the smallest polarizations at brighter craters, suggestive of a less mature surface with a somewhat higher crystalline rock content.

The bland appearance of the polarization ratio images were in stark contrast to color ratio images formed from ultraviolet- and orange-filter data. It was found that bright ray craters and their ejecta were more blue than the surrounding areas by about 12%, while other bright regions were generally more red than darker areas. No color differences could be detected across large scarps, supporting the view that these features were not due to lava flow fronts.

From the albedo and color properties of the surface, Hapke et al. (1975) made a number of conclusions which likely hold true even today: the high brightness and blue color of bright ray craters was inferred to be due to a material which is only weakly absorbing (like feldspar or quartz) and low in Ti, Fe^{3+} and metallic iron. As already pointed out by Murray et al. (1974), the albedo contrast between Mercury's smooth plains and the intercrater and highly cratered units is much smaller than between maria and highlands on the Moon, which implies that the smooth plains may be less abundant in Ti and Fe than the average lunar maria. It was further concluded that no high-Fe, high-Ti maria similar to the lunar counterparts seem to exist on the Mariner 10 hemisphere. These interpretations of the Mariner 10 data signify a surface considerably less similar to the lunar than reported by Murray et al. (1974), who found "surprising similarity to the Moon in regional color variations as well as albedo variations".

Hapke (1977) used brightness profiles along the luminance equator of the Moon and Mercury to derive the average maximum slope angle of the surface. The value for Mercury, about 25 degrees, was shown to be about half that for the Moon, attributed to the effect of the stronger surface gravity of Mercury on the angle of repose of a cohesive soil. Hapke (1977) also showed that the photometric darkening towards the poles detected on both Mercury and lunar far-side images obtained by Mariner 10 could be adequately explained by the effect of crater shadowing, and that the effect is not due to a systematic dependence of normal albedo with latitude. This result implied that the major physical cause of maturation darkening of the surfaces of both bodies is vapor-deposition reduction and formation of submicroscopic metallic iron particles in grain rims due to micrometeoritic impacts, rather than solar wind sputtering. If efficient, the latter effect would likely have produced darkening with a latitude dependency due to the magnetic field strength anisotropy, with large solar wind fluxes being primarily directed towards the polar regions by the inferred dipolar field.

In continuation of the photometric modelling work and its application, Hapke and Wells (1981) showed that a theoretical expression for the bidirectional reflectance of a particulate surface (Hapke 1981) was adequate to explain most of the relative brightness profiles of Mercury as derived from Mariner 10 image data. The model, assuming isotropically single-scattering particles of the same absorption coefficient, still predicted the occurrence of a

strong limb surge which could not be observed for atmosphereless bodies with dark and rough porous regoliths (Hapke 1977). Hapke (1984) presented a rigorous mathematical formalism to take into account the effects on the bidirectional reflectance of macroscopic shadowing on arbitrarily tilted surface sections, and showed that surface roughness angles of 20 degrees could explain the observed absence of a limb surge in Mariner 10 photometric profiles of Mercury.

Further to this work, Bowell et al. (1989) compared and contrasted the photometric models of Hapke (1986 and references therein) and that of Lumme and Bowell (1981 and references therein) and their applications to the Mariner 10 brightness profiles of Mercury and ground-based integral phase curves of Mercury and the Moon. The fits provided by these models were shown to be good and nearly identical, although it was stressed that, due to the number of model parameters and their complex contribution to the brightness of a resolved or integral planetary surface, the solutions are generally not unique.

The highest albedo craters identified by Hapke et al. (1975) were studied by Dzurisin (1977). He proposed that the anomalously bright and structurally well-confined patches on floors of craters 50 km in diameter and larger were caused by an endogenic process as deduced from their morphologic and photometric attributes. This conclusion may suggest that local material, possibly originally subsurface, distinct in the chemical and/or textural properties from the surrounding surface material, may have been extruded through subsurface cracks generated at the impacts.

The Mariner 10 image data from the first inbound trajectory was fully recalibrated by Robinson and Lucey (1997) to remove image artifacts present in the originally reduced data set, in order to study subtle color variations across the surface. Using boundary conditions from ground-based integral phase curve photometry and optical spectroscopy, they removed the photometric function of the resolved disk with the model of Hapke (1986), based on the photometric parameters for the Moon (Helfenstein and Veverka 1987). The derived photometric solution had a mean surface roughness value of 15 degrees, with the other parameters being very lunar-like. Using this recalibration, they found the brightest ray craters to have normal albedos of 0.29, which is twice the global average for the observed hemisphere and considerably lower than previously found by Hapke et al. (1975). The difference could not be explained but was suggested to be due to the improved calibration techniques.

Brightness profiles of Mariner 10 images were reanalyzed by Mallama et al. (2002) and Warell (2004) in a comparison with ground-based photometry of Mercury and the Moon. In modelling the Mariner 10 image data with Hapke's (1993, 2002) bidirectional reflectance function, both authors revealed that the brightness scans were calibrated about 9% too bright compared to ground-based data, which had already been indicated by Hapke et al. (1975). The average surface roughness slope angle was determined to 16 degrees by Mallama from his new extended V-band phase curve observations, and to 8–15 degrees by Warell (2004) from a combination of Mallama's phase curve data and Warell's ground-based disk-resolved images. The smaller range of roughness values found by Warell (2004) was explained as due to light primarily scattered from smooth plains near Mercury's north pole at the very highest phase angles. Values near 15 degrees are consistent with both the Mariner 10 brightness scans and the integral phase curve in general and representative of terrains mainly consisting of cratered highlands and intercrater plains. This difference in surface roughness between geologically different surface units may indicate unique modes of origin, and is consistent with the suggestion that smooth plains are extrusive lava deposits.

Scanned and intensity-corrected photographic copies of Mariner 10 original images were used by Shevchenko (2004, 2006) to study the relative brightnesses and photometric functions of different geologic units. It was found that in a diagram of the value of the photometric function versus the relative image brightness, three types of units are seen as different

trends in the plot. This was interpreted as a result of varying surface roughness caused primarily by particles with different size distributions.

Blewett et al. (2007) used the recalibrated Mariner 10 ultraviolet and orange image data of Robinson and Lucey (1997) to create two spectral parameter images sensitive to the abundance of spectrally neutral opaque phases and the degree of maturity and/or FeO content in the crust. Robinson and Lucey (1997) originally used these images to study plains units with unique properties and argued that one of them, showing low opaque abundance and embayment relations compared to the surroundings, was consistent with the presence of effusive volcanic material. Blewett et al. (2007) performed further work on these data to examine impact-related features across the first encounter incoming hemisphere, and found extended areas of low-opaque material to be present at depth and excavated by some impact craters, as well as small immature craters that had not excavated such low-opaque material. These relations suggested a two-layer crustal model, in which the low-opaque layer is located at a depth of 3–4 km, analogous to the stratification of the lunar highland crust. Furthermore, a location of geologically young but opaque-rich material was found, possibly related to lunar dark-halo impact craters or a pyroclastic deposit origin.

The work of Blewett et al. (2007) must be put in relation to that of Warell and Valegård (2006), who studied similarly constructed spectral parameter images for the poorly known hemisphere obtained with data from 1-m Swedish Solar Telescope (see Ksanfomality, this volume). Though the spatial resolution was two orders of magnitude lower than that of Mariner 10 images, one advantage was the extended near-infrared spectral coverage allowing separation of the maturity/FeO ambiguity. It appears that geologic features similar to those identified on the Mariner 10 hemisphere are also present on the less-known hemisphere particularly with respect to opaque-rich and mature areas. Such findings are consistent with the presence of more iron- and titanium-rich material that may have been excavated from depth. If so, volcanic plains may have formed at locations scattered globally across the surface of Mercury.

5.1.1 The Extreme Ultraviolet Albedo of Mercury's Surface

The UV albedos of Mercury's surface were measured by the Mariner 10 UV spectrometer (Broadfoot et al. 1976; Wu and Broadfoot 1977) and, at the first encounter, were found to be similar to the UV albedo of the Moon (Broadfoot et al. 1974). Further detailed analysis after the second and third encounters showed Mercury's surface to be of considerably lower albedo as shown in Fig. 6, for Mercury and in Fig. 7 for the ratio of Mercury's albedo to that of the Moon.

Although there are uncertainties in the absolute geometric albedo as shown by error bars in the EUV albedo, the values of the ratio of Mercury to the Moon are thought to be quite good because instrumental systematic errors are removed by the ratio technique.

5.2 Material Properties

Measurements carried out with the Mariner 10 infrared radiometer provided information on the temperature and thermal properties of the crust (Chase et al. 1976). Observations were made on the first pass and primarily the unilluminated hemisphere was observed. It was found that Mercury is essentially indistinguishable from the Moon, with the derived thermal skin depth, electric skin depth and dielectric loss tangent all within the ranges found for the Moon. Observed variations in the derived surface temperature along the scan direction was attributed to differences in thermal inertia and rock coverage. One of the local enhancements

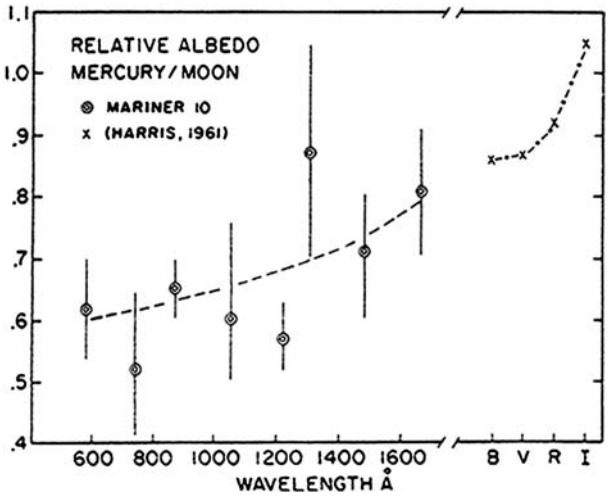

Fig. 7 The relative geometric EUV albedos of Mercury and the Moon as measured by the UV spectrograph on Mariner 10 and from Harris (1961)

of thermal inertia, found to display strong radar backscattering properties by Zohar and Goldstein (1974), was interpreted as due to a young ray crater. With respect to rock coverage, it was estimated that most of the surface was covered with about 2% exposed bare rock, while for some local hot regions the rock coverage was estimated to be up to a few times greater. Based on the relation between the loss tangent and the measured ilmenite content in lunar soil samples found by Olheoft and Strangway (1975), the estimated loss tangent of Mercury implied about 20% FeO + TiO_2 present in the crust. The results of ground-based cm wavelength observations of Mercury's surface and subsequent modelling of thermal and dielectric properties of the regolith by Mitchell and de Pater (1994) present quite a different view of Mercury's surface chemistry. The entire suite of ground-based observations puts an upper limit of 3% for FeO and TiO2 in Mercury's regolith. This subject is discussed in detail by Sprague et al. (2007, this volume),

6 Topography

The space exploration of terrestrial planets has recently demonstrated the importance of 3D rendering of planetary surfaces (e.g. Barnett and Nimmo 2002; Watters et al. 2002; Watters 2003; Neukum et al. 2004; Plescia 2004). Morphology is of paramount importance for better defining the main geological units of the planets, structural features linked to global and local tectonics, impact crater populations and, if present, volcanic edifices.

Then a digital elevation model (DEM) is needed when correcting images for illumination effects because it allows accurate calculation of incidence, emission, and phase angles on a pixel-by-pixel basis.

Up to now there are very few studies on the Mercury topography due to the small data set and the quite poor quality of the images to perform stereo reconstruction, in terms of spatial resolution, solar illumination, and view angles.

During all three flybys the same hemisphere and illumination conditions were presented to Mariner 10. Some of the images overlap and were taken from widely separated viewpoints, thus providing stereo coverage. Example stereo images (Davies et al. 1978) and a catalog of stereo pairs (Jet Propulsion Laboratory (JPL) 1976) have been published. How-

ever, at the time that these stereo pairs were published, the camera position and orientation data were still preliminary, and some of these pairs have extremely weak stereo.

Further interesting work was done by Cook and Robinson (2000) that used newly refined camera position and orientation data (Davies et al. 1996; Robinson et al. 1997, 1999a), finding additional useful stereo pairs never before identified. They compiled a new catalog of stereo pairs and produced a map of stereo coverage (Robinson et al. 1999b). They were able to provide approximately 24% of the planet mapped topographically to better than ± 1 km height accuracy (for a single matched point), and 6% of the surface mapped to better than ± 400 m height accuracy.

Recently, Andre' et al. (2005) used image pairs from the Mariner 10 data set to make stereo reconstructions of the Beethoven and Tolstoj basins from which they concluded that their topography is similar to that of lunar-mare filled basins. These maps are, however, coarse. Laser altimetry and dedicated stereo imaging from the MESSENGER and Bepi-Colombo space missions will provide high spatial resolution products at better than 10 m vertical accuracy. A Digital Terrain Model—with a grid size lower than 300 m—of the entire planet surface; will also be implemented using new technologies and stereo reconstruction techniques. At present, there is no adequate analog. Clementine data from the Moon was too poor to be used for this purpose.

References

S.L. Andre', T.R. Watters, Proc. Lunar Planet. Sci. Conf. [CDROM], 37th, abstract 2054 (2006)
S.L. Andre', T.S. Watters, M.S. Robinson, Geophys. Res. Lett. **32**, L21202 (2005)
D.N. Barnett, F. Nimmo, Icarus **157**, 42 (2002)
D.T. Blewett, B.R. Hawke, P.G. Lucey, M.S. Robinson, J. Geophys. Res. **112**, 2005 (2007)
E. Bowell, B. Hapke, D. Domingue, K. Lumme, J. Peltoniemi, A.W. Harris, *Asteroids II, Proc. of the Conference* (University of Arizona Press, Tucson, 1989), p. 524
A.L. Broadfoot, S. Kumar, M.J.S. Belton, M.B. McElroy, Science **185**, 166 (1974)
A.L. Broadfoot, D.E. Shemansky, S. Kumar, Geophys. Res. Lett. **3**, 580 (1976)
S.C. Chase Jr., E.D. Miner, D. Morrison, G. Muench, G. Neugebauer, Icarus **28**, 565 (1976)
A.C. Cook, M.S. Robinson, J. Geophys. Res. **105**, 9429 (2000)
M.E. Davies, S.E. Dwornik, D.E. Gault, R.G. Strom, *Atlas of Mercury*. NASA Spec. Publ., vol. SP-423 (1978), p. 127
M.E. Davies, T.R. Colvin, M.S. Robinson, K. Edwards, Bull. Am. Astron. Soc. **28**, 1115 (1996)
D. Dzurisin, Geophys. Res. Lett. **4**, 383 (1977)
D.E. Gault, J.E. Guest, J.B. Murray, D. Dzurisin, M.C. Malin, J. Geophys. Res. **80**, 2444 (1975)
B. Hapke, Astron. J. **71**, 386 (1966)
B. Hapke, Conference on Comparisons of Mercury and the Moon, Houston, TX, Nov. 15–17 (1977)
B. Hapke, J. Geophys. Res. **86**, 3039 (1981)
B. Hapke, Icarus **59**, 41 (1984)
B. Hapke, Icarus **67**, 264 (1986)
B. Hapke, *Theory of Reflectance and Emittance Spectroscopy* (Cambridge University Press, Cambridge, 1993)
B. Hapke, Icarus **157**, 523 (2002)
B. Hapke, E. Wells, J. Geophys. Res. **86**, 3055 (1981)
B. Hapke, G.E. Danielson Jr., K. Klaasen, L. Wilson, J. Geophys. Res. **80**, 2431 (1975)
D. Harris, in *Planets and Satellites*, ed. by G. Kuiper, B. Middlehurst (University of Chicago Press, Chicago, 1961), pp. 273–342
W.K. Hartmann, G. Neukum, Space Sci. Rev. **96**, 165 (2001)
P. Helfenstein, J. Veverka, Icarus **72**, 342 (1987)
B.A. Ivanov, Space Sci. Rev. **96**, 87 (2001)
B.A. Ivanov, G. Neukum, R. Wagner, Workshop on Mercury: Space Environment, Surface, and Interior, Chicago, IL, 2001, p. 65
Jet Propulsion Laboratory (JPL), MVM '73 stereo data package user guide. Pasadena, CA, 1976
K. Lumme, E. Bowell, Astron. J. **86**, 1694 (1981)

A. Mallama, D. Wang, R.A. Howard, Icarus **155**, 253 (2002)
D. Mitchell, I. de Pater, Icarus **110**, 2–32 (1994)
B.C. Murray, M.J.S. Belton, G.E. Danielson, M.E. Davies, D.E. Gault, B. Hapke, B. O'Leary, R.G. Ström, V. Suomi, N. Trask, Science **185**, 169 (1974)
J.F. McCauley, G.G. Guest, J.E. Schaber, N.J. Trask, R. Greeley, Icarus **47**, 184 (1981)
H.J. Melosh, W.B. McKinnon, in *Mercury*, ed. by F. Vilas, C.R. Chapman, M.S. Matthews (University of Arizona Press, Tucson, 1988), p. 374
G. Neukum, Meteoritenbombardement and Datierungplanetarer Oberachen. Habilitation Dissertation for faculty membership. Univ. of Munich, 1983, p. 186
G. Neukum, B.A. Ivanov, in *Hazards Due to Comets and Asteroids*, ed. by T. Gehrels (Univ. of Arizona Press, Tucson, 1994), p. 359
G. Neukum, B.A. Ivanov, W.K. Hartmann, Space Sci. Rev. **95**, 55 (2001)
G. Neukum, R. Jaumann, H. Hoffmann, E. Hauber, J.W. Head, A.T. Basilevsky, B.A. Ivanov, S.C. Werner, S. van Gasselt, J.B. Murray, T. McCord, The HRSC Co-Investigator Team, Nature **432**, 979 (2004)
F. Nimmo, T.R. Watters, Gephys. Res. Lett. **31**, L02701 (2004). doi:10.1029/2003GL018847
G.R. Olheoft, D.W. Strangway, Earth Planet. Sci. Lett. **24**, 394 (1975)
R.J. Pike, in *Mercury*, ed. by F. Vilas, C.R. Chapman, M.S. Matthews (The University of Arizona Press, Tucson, 1988), p. 165
J.B. Plescia, J. Geophys. Res. **109**, E03003 (2004). doi:10.1029/2002JE002031
M. Robinson, P.G. Lucey, Science **275**, 197 (1997)
M.S. Robinson, M.E. Davies, T.R. Colvin, K.E. Edwards, *Proc. Lunar Planet. Sci. Conf., 28th*, 1997, pp. 1187–1188
M.S. Robinson, M.E. Davies, T.R. Colvin, K.E. Edwards, J. Geophys. Res. **104**, 30852 (1999a)
M.S. Robinson, A.S. McEwen, E. Eliason, E.M. Lee, E. Malaret, P.G. Lucey, *Proc. Lunar Planet. Sci. Conf.* [CDROM], 30th, abstract 1931, 1999b
V.V. Shevchenko, Sol. Syst. Res. **38**, 441 (2004)
V.V. Shevchenko, Adv. Space Res. **38**, 589 (2006)
P.H. Shultz, D.E. Gault, NASA Tech. Memo., X-62 (388) (1974)
J.M. Soha, D.J. Lynn, J.J. Lorre, J.A. Mosher, N.N. Thayer, D.A. Elliott, W.D. Benton, R.E. Dewar, J. Geophys. Res. **80**, 2394 (1975)
P.D. Spudis, J.E. Guest, in *Mercury*, ed. by F. Vilas, C.R. Chapman, M.S. Matthews (The University of Arizona Press, Tucson, 1988), p. 118
R.G. Strom, N.J. Trask, J.E. Guest, J. Geophys. Res. **80**(7), 2478 (1975)
R.G. Ström, G. Neukum, in *Mercury*, ed. by F. Vilas, C.R. Chapman, M.S. Matthews (The University of Arizona Press, Tucson, 1988), p. 336
R.G. Ström, R. Malhotra, T. Ito, F. Yoshida, D.A. Kring, Science **309**, 1847 (2005)
R.G. Strom, A.L. Sprague, *Exploring Mercury: The Iron Planet* (Springer, Praxis, Chichester, 2003), p. 216
P.G. Thomas, P. Masson, L. Fleitout, in *Mercury*, ed. by F. Vilas, C.R. Chapman, M.S. Matthews (University of Arizona Press, Tucson, 1988), p. 401
P.G. Thomas, Planet. Space Sci. **45**, 3 (1997)
R.J. Wagner, U. Wolf, B.A. Ivanov, G. Neukum, Workshop on Mercury: Space Environment, Surface, and Interior. Chicago, IL, 2001, p. 106
J. Warell, Icarus **167**, 271 (2004)
J. Warell, P.-G. Valegård, Astron. Astrophys. **460**, 625 (2006)
T.R. Watters, R.S. Schultz, M.S. Robinson, A.C. Cook, Geophys. Res. Lett. **29**(11), 1542 (2002). doi:10.1029/2001GL014308
T.R. Watters, J. Geophys. Res. **108**, 5054 (2003). doi:10.1029/2002JE001934
T.R. Watters, M.S. Robinson, C.R. Bina, P.D. Spudis, Geophys. Res. Lett. **31**, L04701 (2004). doi:10.1029/2003GL019171
H.H. Wu, A.L. Broadfoot, Geophys. Res. Lett. **82**, 759–760 (1977)
S. Zohar, R.M. Goldstein, Astron. J. **79**, 85 (1974)